

# Joint $L^1$ and Total Variation Regularization for Magnetic Detection Electrical Impedance Tomography

Liling Hao and Lisheng Xu

Department of SINO-DUTCH Biomedical and Information Engineering  
Northeastern University, Shenyang, 110169, China  
haoll@bmie.neu.edu.cn, xuls@bmie.neu.edu.cn

**Abstract** — Magnetic detection electrical impedance tomography (MDEIT) is an imaging modality that aims to compute the cross-sectional distribution of the conductivity of a volume from the magnetic flux density surrounding the object. Owing to the Biot-Savart law, the MDEIT inverse problem is inherently ill-conditioned making image reconstruction highly susceptible to the effects of noise and numerical errors. Appropriate priors or penalties are needed to facilitate reconstruction and to restrict the search space to a specific solution set. The images have the sparsity property and sharp variations. Consequently, this paper presents an approach involving a combination of the  $L^1$  and total variation norm penalties, the former to suppress spurious background signals and enforce sparsity and the latter to preserve local smoothness and piecewise constancy in the MDEIT reconstructed images. The primal dual-interior point method (PD-IPM) for minimizing the joint  $L^1$ -TV penalty was used in the paper. The method was validated by using MDEIT simulated data and experimental data in comparison with the performances of the  $L^2$ ,  $L^1$  and total variation norm penalty-based approaches. The results show that the joint  $L^1$ -TV regularized algorithm preserves sparsity property, local smoothness and piecewise constancy, leading to improvements in the localization of the reconstructed images in MDEIT.

**Index Terms** — Inverse problem, joint regularization,  $L^1$  norm, magnetic detection electrical impedance tomography, total variation.

## I. INTRODUCTION

Magnetic detection electrical impedance tomography (MDEIT) is an experimental imaging modality that aims to reconstruct electrical conductivity images from the magnetic flux density surrounding the object induced by an injected current. Since measurements of the magnetic flux density surrounding the object don't require surface contact, MDEIT can record a greater number of measurements with precise detector positions. While electrical impedance tomography (EIT) records the surface voltage by electrodes on the surface, leading to

the more errors in the measurement and less number of measurements. As a different type of EIT, MDEIT overcomes the shortcomings of the standard EIT and retains its merits. MDEIT also has some comparative advantages over other similar imaging techniques in some respects. Magnetic resonance impedance tomography (MREIT) eliminates some of the principle advantages of EIT, such as low cost and the potential for long-time monitoring. Magnetic induction tomography (MIT) has limitation in the biomedical application due to the smaller signal produced by the eddy current compared to the signal produced by the injected current.

The concept of MDEIT was introduced in 1992 by Ahlfors and Ilmoniemi. They proposed a method that determines the conductivity distribution within an object using magnetic field measurements, which called magnetic impedance tomography (MIT) [1]. The feasibility of using magnetic field measurements to produce current density images was demonstrated with four examples in two dimensions, and made the first step towards developing MIT as a new medical imaging technique [2]. Then, this technique was called as MDEIT, because original name was easily confused with magnetic induction tomography [3]. They applied the Tikhonov regularization and truncated singular value method (TSVD) to MDEIT current density reconstruction. Ireland described a method of iterative grid refinement, improving the ill-posed nature of the MDEIT inverse problem by limiting the number of unknowns to be solved [4]. But they just constructed the current density image, the conductivity distribution reconstruction leaved to be solved. In this work we construct the conductivity image using simulated data.

The inverse problem of MDEIT is ill-posed. Consequently regularization techniques have been adopted to stabilize the solution [2-4]. However, these  $L^2$  norm regularization methods limit the capability of describing sharp variations in the conductivity and tend to smooth out edges in images. The human images have well defined organ boundaries that present sharp transitions in conductivity. The ability of reconstructing sharp changes should lead to a better estimation of the

boundaries and a better accuracy in the estimated values. Sharp images could better identify the boundaries between the regions. The  $L^2$  norm algorithms blur such contrasts and make more difficult to estimate the size and the contrast value. These inspire us to investigate a regularization method that preserves the edge information of the reconstructed conductivity image.

The total variation (TV) minimizing function regularization preserves discontinuities in the reconstructed profiles [5]. The TV is defined as the  $L^1$  norm of the differences between neighbouring pixels. This particular form of the TV penalty enforces sparsity on pixel differences and consequently tends to generate images with piecewise constant regions and sharp boundaries. As a result, we studied TV regularization strategy and showed its superiority over the conventional  $L^2$  regularization in our previous work [6]. However, in some cases, the images tend to be very sparse with some locally smooth high value regions. For example, the cancer is the localized high impedance tissue. Another application is the difference imaging, where the goal of the reconstruction is to recover the conductivity difference that commonly exhibits the sparsity. The  $L^1$  norm is often used to enforce sparsity in images and is particularly popular in the field of compressed sensing [7-8]. But it tends to shrink the support of large or non-sparse sources. The TV regularization can preserve the boundary of large object well while removing small features and sparse sources. This inspires us to joint  $L^1$  norm penalty and TV penalty, enforcing sparsity and smoothness in the reconstructed images. The similar methods have recently been applied to microwave imaging [9] and fluorescence molecular tomography [10-11]. This paper firstly uses the joint  $L^1$  and total variation regularization to solve the inverse problem of magnetic detection electrical impedance tomography. In this work, the primal dual-interior point method (PD-IPM) was applied to minimize the joint  $L^1$ -TV penalty.

## II. METHODS

MDEIT is technically based on generating a current distribution inside of the object by injecting an alternating current, at one of a range of frequencies, into a conducting object with surface electrodes. A large number of magnetic flux density measurements recorded with magnetic field sensors at fixed positions around the object are used to reconstruct the conductivity distributions on tomographic planes.

### A. Inverse problem of MDEIT

A straightforward approach for solving the inverse problem of MDEIT is seeking the optimal solution by minimizing the cost function which is the residual norm between the calculated data and the measured data. The resulting optimization problem is as follows:

$$\hat{\boldsymbol{\sigma}} = \arg \min_{\boldsymbol{\sigma}} \frac{1}{2} \|F(\boldsymbol{\sigma}) - \mathbf{B}\|_2^2, \quad (1)$$

where  $F(\boldsymbol{\sigma})$  is the forward operator calculated at the conductivity  $\boldsymbol{\sigma}$ , and  $\mathbf{B}$  is the measured magnetic field. The reconstruction algorithm is capable of finding relative conductivity distribution only. Yet, the inverse problem of MDEIT is ill-posed, making the image reconstruction highly sensitive to the noise of the measurement data and numerical errors, and necessitating the use of regularization. The forward operator  $F(\boldsymbol{\sigma})$  can be stated as [12]:

$$F(\boldsymbol{\sigma}) = \frac{\mu_0}{4\pi} \cdot \int_{\Omega} -\boldsymbol{\sigma} \nabla \varphi \times \frac{(\mathbf{r} - \mathbf{r}')}{|\mathbf{r} - \mathbf{r}'|^3} d\mathbf{r}'. \quad (2)$$

The Jacobian matrix  $\mathbf{A}$  is defined as:

$$\mathbf{A} = \frac{\partial F(\boldsymbol{\sigma})}{\partial \boldsymbol{\sigma}} = \frac{\partial F(\boldsymbol{\sigma})}{\partial \mathbf{J}} \cdot \frac{\partial \mathbf{J}}{\partial \boldsymbol{\sigma}}, \quad (3)$$

with

$$\frac{\partial \mathbf{J}}{\partial \sigma_j} = \frac{\partial(-\boldsymbol{\sigma} \nabla \varphi)}{\partial \sigma_j} = -(\nabla \varphi)_j - \boldsymbol{\sigma} \frac{\partial(\nabla \varphi)}{\partial \sigma_j}. \quad (4)$$

Alternate the index of partial derivative in  $\partial \nabla \varphi / \partial \sigma$ , and obtain the following equation:

$$\frac{\partial \mathbf{J}}{\partial \sigma_j} = -(\nabla \varphi)_j - \boldsymbol{\sigma} \nabla \frac{\partial \varphi}{\partial \sigma_j}. \quad (5)$$

The partial derivative of electrical potential to conductivity  $\partial \varphi / \partial \sigma$  can be calculated through the linear equation system of the forward problem. Calculate the partial derivative to the conductivity  $\boldsymbol{\sigma}$ , and obtain the following equation:

$$\frac{\partial \varphi}{\partial \sigma_j} = -\mathbf{S}^{-1} \cdot \frac{\partial \mathbf{S}}{\partial \sigma_j} \cdot \varphi, \quad (6)$$

where  $\mathbf{S}$  is the coefficient matrix between the excitation matrix and the nodal voltage matrix based on the finite element method.

### B. Joint $L^1$ and total variation regularization

The cost function we seek to minimize contains three parts—a data-fitting term, a sparsifying penalty term and a smoothing penalty term. The sparsifying penalty under consideration is the  $L^1$  norm of the conductivity image  $\boldsymbol{\sigma}$ . The cost function is:

$$\hat{\boldsymbol{\sigma}} = \arg \min_{\boldsymbol{\sigma}} f(\boldsymbol{\sigma}) = \arg \min_{\boldsymbol{\sigma}} \frac{1}{2} \|F(\boldsymbol{\sigma}) - \mathbf{B}\|_2^2 + \lambda_{L^1} \|\boldsymbol{\sigma}\|_1 + \lambda_{TV} \sum_i \sqrt{|\mathbf{L}_i \boldsymbol{\sigma}|^2 + \delta}, \quad (7)$$

where  $\delta$  is a constant with a small positive value, which enforces the differentiability of the TV penalty.  $\mathbf{L}$  is a regularization matrix.  $\lambda_{L^1}$  and  $\lambda_{TV}$  are the regularization parameter for  $L^1$  regularization and TV regularization,

respectively.

Primal Dual-Interior Point Method (PD-IPM) was utilized for minimizing the joint  $L^1$ -TV penalty [13-14]. The joint  $L^1$ -TV regularized inverse problem can be formulated as:

$$(P) \arg \min_{\boldsymbol{\sigma}} \frac{1}{2} \|F(\boldsymbol{\sigma}) - \mathbf{B}\|_2^2 + \lambda_{L^1} \|\boldsymbol{\sigma}\|_1 + \lambda_{TV} \sum_i |\mathbf{L}_i \boldsymbol{\sigma}| \quad (8)$$

We call Equation (8) primal problem and label it (P), where  $\boldsymbol{\sigma}$  is the primal variable. An equivalent problem to (P) is called dual problem which is a maximization problem:

$$(D) \max_{\mathbf{x}: |x_i| \leq 1} \min_{\boldsymbol{\sigma}} \frac{1}{2} \|F(\boldsymbol{\sigma}) - \mathbf{B}\|_2^2 + \lambda_{L^1} \|\boldsymbol{\sigma}\|_1 + \lambda_{TV} \sum_i x_i \mathbf{L}_i \boldsymbol{\sigma}, \quad (9)$$

where  $\mathbf{x}$  is the dual variable. The complementarity condition is:

$$|\mathbf{L}_i \boldsymbol{\sigma}| - x_i \sqrt{|\mathbf{L}_i \boldsymbol{\sigma}|^2 + \delta} = 0 \quad i=1, \dots, n, \quad (10)$$

with the feasibility conditions,

$$\begin{aligned} |x_i| &\leq 1 \quad i=1, \dots, n \\ \mathbf{A}^T (F(\boldsymbol{\sigma}) - \mathbf{B}) + \lambda_{L^1} \mathbf{1} + \lambda_{TV} \mathbf{L} \mathbf{x} &= 0 \end{aligned} \quad (11)$$

Apply the Gauss Newton method and obtain the updates of the primal and dual variables:

$$\begin{aligned} \Delta \boldsymbol{\sigma}_k &= -(\mathbf{A}_k^T \mathbf{A}_k + \lambda_{TV} \mathbf{L}^T \mathbf{P}_k^{-1} \mathbf{Q}_k \mathbf{L})^{-1} \\ &\quad \cdot [\mathbf{A}_k^T (F(\boldsymbol{\sigma}_k) - \mathbf{B}) + \lambda_{L^1} \mathbf{1} + \lambda_{TV} \mathbf{L}^T \mathbf{P}_k^{-1} \mathbf{L} \boldsymbol{\sigma}_k], \\ \Delta \mathbf{x}_k &= -\mathbf{x}_k + \mathbf{P}_k^{-1} \mathbf{L} \boldsymbol{\sigma}_k + \mathbf{P}_k^{-1} \mathbf{Q}_k \mathbf{L} \Delta \boldsymbol{\sigma}_k \end{aligned} \quad (12)$$

with

$$\begin{aligned} \eta_i^k &= \sqrt{|\mathbf{L}_i \boldsymbol{\sigma}_k|^2 + \delta} \\ \mathbf{P}_k &= \text{diag}(\eta_i^k) \\ \mathbf{Q}_k &= \text{diag}\left(1 - \frac{x_i^k \mathbf{L}_i \boldsymbol{\sigma}_k}{\eta_i^k}\right) \end{aligned} \quad (13)$$

Moreover, for maintaining dual feasibility, we calculate the exact value of step length according to the step rule:

$$\mathbf{x}_{k+1} = \mathbf{x}_k + \min(1, \phi^*) \Delta \mathbf{x}_k, \quad (14)$$

where  $\phi^*$  is a scalar value such that,

$$\phi^* = \sup\{\phi: |x_{ki} + \phi \Delta x_{ki}| \leq 1, i=1, \dots, n\}. \quad (15)$$

With joint  $L^1$  and TV penalties, there are two regularization parameters to be selected. These parameters were empirically determined by sweeping them over a range of values. The sparsifying and smoothing effects increase as we increase the weights on the  $L^1$  and TV penalties, respectively.

### III. EXPERIMENTS AND RESULTS

We tested the joint  $L^1$ -TV regularization approach and compared it with the  $L^1$ , TV and  $L^2$  penalties using simulated and experimental data.

#### A. Simulation results

In the section, we evaluated the performance of the joint  $L^1$ -TV regularization algorithm and compared its performance with the  $L^1$ , TV and  $L^2$  penalties. The evaluation was conducted on the simulated data. The simulated phantom is shown in Fig. 1 (a). Suppose a 10 mA current was injected by one pair of opposite electrodes and the size of the electrode is just the same as the area of an element. The total element number is 2160 for simulating the magnetic flux density data (forward model) and 540 for the image reconstruction (inverse model). The positions of the magnetic flux density measurement coils at 120 equally spaced angles along 3 equally spaced circles surrounding the circular imaging object, which results 360 measurements in all, are displayed in Fig. 1 (b). In this paper, the numerical treatment was applied to the singular values of the sensitivity matrix in the presence of noisy measurements, subsequently suggesting the optimal detector configurations [15]. For the simulated phantom, only magnetic flux density  $B_z$  can be recorded by coil at these positions. So the orientations of coils are displayed as Fig. 1 (b).

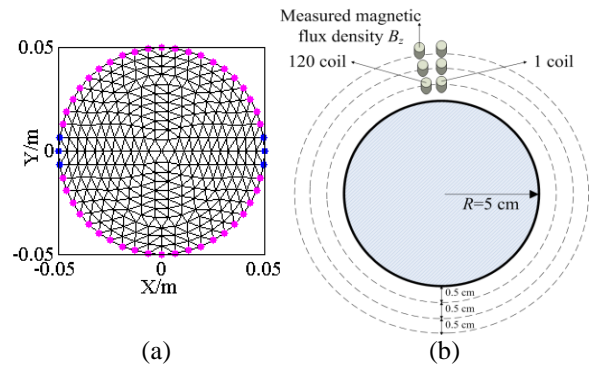


Fig. 1. The simulated phantom used for generating the simulated data. (a) The opposite electrodes covering 2 elements located in the horizontal direction, (b) the diagram displaying the positions of the magnetic flux density measurement coils at 120 equally spaced angles along 3 equally spaced circles surrounding the circular imaging object, and orientations for the measured magnetic flux density  $B_z$ .

The hypersensitivity near the boundary results in the better resolution of inhomogeneity near the boundary,

while the insensitivity in the centre leads to a worse resolution of inhomogeneity in the centre. For the different regularizations, the differences among the reconstructed conductivity distributions may be smaller for the inhomogeneity in the centre, and be bigger for the inhomogeneity near the boundary. In order to better test the performance of the joint  $L^1$ -TV regularization, we selected three simulation models with the conductivity distributions as shown in Fig. 2 (a), Fig. 3 (a) and Fig. 4 (a). We set the background conductivity for 0.1 S/m, the small inclusions present the same value of 0.2 S/m. In actual measurements, there will be some necessary noise. White Gaussian noise with a signal-to-noise (SNR) of 60 dB was added to the simulated magnetic flux density data to make the simulations realistic.

For the model 1 with inhomogeneity near the boundary, the reconstruction results for  $L^2$ ,  $L^1$ , TV and joint  $L^1$ -TV penalties are shown in Fig. 2 (b)–(e), respectively. This figure clearly indicates the  $L^2$  penalty generates the most blurred solution and the most mean background signal level. The  $L^1$  penalty suppresses spurious background and enforces sparsity. The TV penalty preserves the edge. The joint  $L^1$ -TV penalty simultaneously encourages properties of sparsity and smoothness in the reconstructed image. The  $L^1$ , TV and the joint  $L^1$ -TV schemes lead to significantly stronger mean signal levels over the region of interest (ROI) than the  $L^2$  penalty. The result obtained using the joint  $L^1$ -TV penalty is most similar to the conductivity image displayed in Fig. 2 (a).

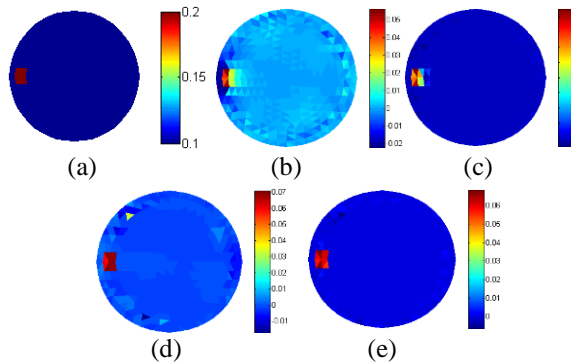


Fig. 2. The reconstructed results of model 1 with inhomogeneity near the boundary. (a) Conductivity map, (b) the reconstructed image using  $L^2$  norm penalty, (c) the reconstructed image using the  $L^1$  norm penalty, (d) the reconstructed image using TV penalty, and (e) the reconstructed image using both  $L^1$  and TV penalties.

For the model 2 with inhomogeneity in the centre, the reconstructed results are shown in Fig. 3. The  $L^2$  and the TV schemes led to the worse resolution of inhomogeneity than the model 1. The  $L^1$  and the joint  $L^1$ -TV approaches generated the least mean background

signal level, while the joint  $L^1$ -TV approach yielded a lower background standard deviation than the  $L^1$  and TV penalties individually.

The reconstructed results of the model 3 with two small inclusions are presented in Fig. 4, where the reconstructed images are shown for different regularizations. The joint  $L^1$ -TV penalty was observed to yield the best result, which preserves local smoothness and piecewise constancy with TV penalty and simultaneously encourages properties of sparsity and eliminates the artifacts between the two small inclusions with  $L^1$  norm approach.

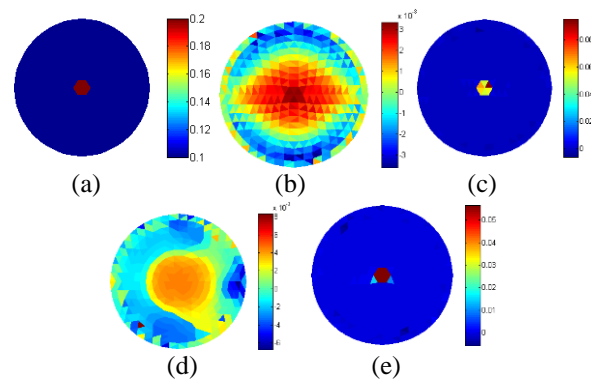


Fig. 3. The reconstructed results of model 2 with inhomogeneity in the centre. (a) Conductivity map, (b) the reconstructed image using  $L^2$  norm penalty, (c) the reconstructed image using the  $L^1$  norm penalty, (d) the reconstructed image using TV penalty, and (e) the reconstructed image using both  $L^1$  and TV penalties.

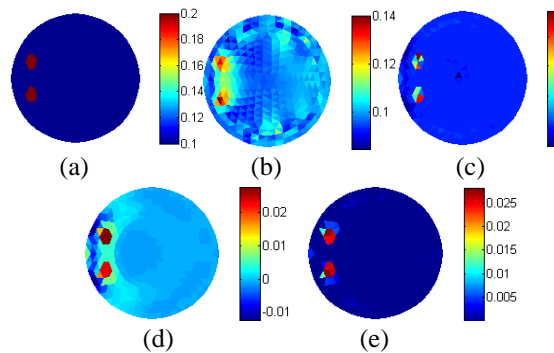


Fig. 4. The reconstructed results of model 3 with two small inclusions. (a) Conductivity map, (b) the reconstructed image using  $L^2$  norm penalty, (c) the reconstructed image using the  $L^1$  norm penalty, (d) the reconstructed image using TV penalty, and (e) the reconstructed image using both  $L^1$  and TV penalties.

## B. Current density image reconstruction experiment

In order to test the performance of joint regularized algorithm for the realistic magnetic field data, a discrete

phantom consisting of one conducting rod of length 1.2 m in free space was used (Fig. 5 (a)). The coil was used to record the magnetic field measurements made with an injected current of 10 mA at 31.25 kHz. Fig. 5 (b) presents the axial current density distribution of the imaging area with a 5 cm radius. The magnetic field data was measured on a perpendicular plane surrounding the object in the middle height of the object. The position of the measurement point on the perpendicular plane at 36 equally spaced angles along 3 equally spaced circles surrounding the circular imaging object, which results 108 measurements in all, is shown in the Fig. 5 (c). The orientation of coil at each angle was tangent to the circle region of interest at every point. The data recorded by the coil was amplified by a low-noise amplifier, and then fed to the data acquisition board NI-PCI6281 produced by National Instruments. The SNR of voltage acquired by the data acquisition board was 42-57 dB. The digital voltage data was processed by the digital lock-in amplifier to filter the noise and produce the amplitude of the voltage. Fig. 6 presents the vector graphics of the simulated and measured magnetic flux density. The mean difference between the measured and simulated data is 4.08%, with values ranging from 0.55% to 8.74%.

The region of the imaging object was meshed into 316 elements. We reconstructed the current density image at the 316 positions from the 108 external magnetic field measurements. For the current density image presented in the paper (Fig. 5 (b)), it has sparsity and sharp edges. The joint  $L^1$ -TV penalty was used to reconstruct the current density image for this ill-posed inverse problem, enforcing sparsity and preserving local smoothness and piecewise constancy in the reconstructed images.

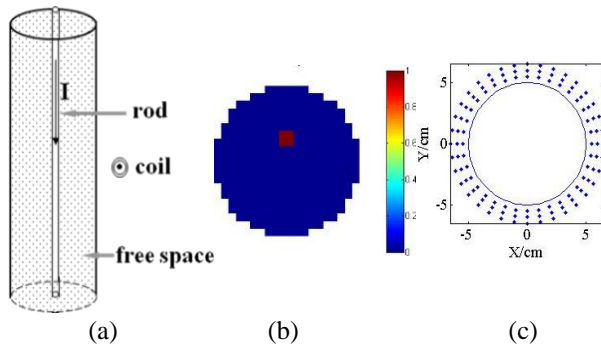


Fig. 5. The magnetic field measurement configuration. (a) The discrete phantom consisting of one conducting rod with an injected current, (b) the original current density distribution of the imaging object, and (c) the positions of the magnetic flux density measurement points on a perpendicular plane surrounding the object in the middle height of the object.

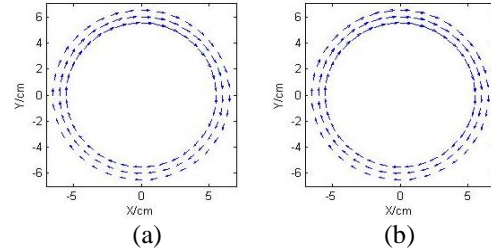


Fig. 6. The vector graphics of the simulated and measured magnetic field, which display the magnetic flux density as arrows at the measurement points. The length of arrows represents the magnitude of magnetic field, while the direction of arrow corresponds to the direction of the magnetic field. (a) The vector graphic displaying the simulated magnetic field, and (b) the vector graphic displaying the measured magnetic field.

Figure 7 shows the reconstructed current density images for  $L^2$ ,  $L^1$ , TV and joint  $L^1$ -TV penalties, using the simulated magnetic field data with 50 dB white Gaussian noise. The commonly used  $L^2$  penalty generates the most blurred solution. The  $L^1$  penalty suppresses spurious background and enforces sparsity, but reduces the object region. The TV penalty preserves the edge, but enlarges the object region. The joint  $L^1$ -TV penalty simultaneously encourages properties of sparsity and smoothness in the reconstructed image. The result obtained using the joint  $L^1$ -TV penalty is most similar to the current density image displayed in Fig. 5 (b).

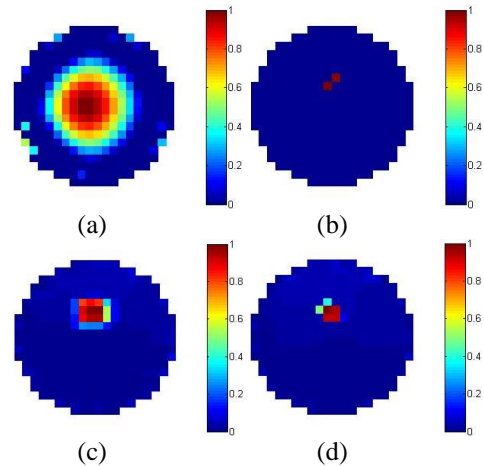


Fig. 7. The reconstructed current density images from the simulated magnetic field data with 50 dB white Gaussian noise. (a) The reconstructed image using  $L^2$  norm penalty, (b) the reconstructed image using the  $L^1$  norm penalty, (c) the reconstructed image using TV penalty, and (d) the reconstructed image using both  $L^1$  and TV penalties.

Based on the experimental data, we employed the  $L^2$ ,  $L^1$ , TV and joint  $L^1$ -TV penalties to reconstruct the current density images shown in Fig. 8. Using  $L^1$  or TV regularization, in combination or separately, clearly leads to improvements in localizing the inhomogeneity in MDEIT. There is less difference between the  $L^1$ , TV and joint  $L^1$ -TV images than between any of these and  $L^2$  image. The joint  $L^1$ -TV images have the most natural appearance in the simulated and experimental results.

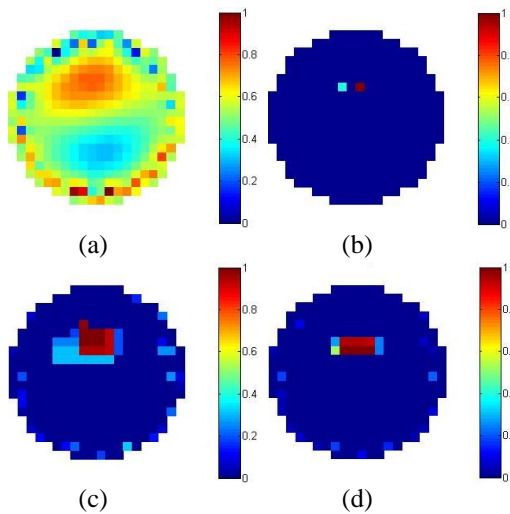


Fig. 8. The reconstructed current density images from the experimental magnetic field data. (a) The reconstructed image using  $L^2$  norm penalty, (b) the reconstructed image using the  $L^1$  norm penalty, (c) the reconstructed image using TV penalty, and (d) the reconstructed image using both  $L^1$  and TV penalties.

## VI. CONCLUSION

In this work, the joint  $L^1$ -TV regularization was applied to the inverse problem of magnetic detection electrical impedance tomography. We used the primal dual-interior point method for efficiently minimizing joint  $L^1$ -TV penalty, and compared its performance with the  $L^2$  norm,  $L^1$  norm and TV regularizations. Through the simulations of differential conductivity image reconstructions, it showed that the joint  $L^1$ -TV regularization preserved sparsity, discontinuities and piecewise constancy in the reconstructed image.

For the experiment of current density image reconstruction, the joint  $L^1$ -TV penalty reconstructed the more accurate current density image than either  $L^1$  penalty or TV penalty. Moreover, all of these performed better than the conventional  $L^2$  penalty. The simulated and experimental results of the current density image reconstruction appeared similar, but the simulation result was little better than the experimental result. The possible reason of the difference in results is as follow. The sources of inaccuracy in simulation result are noise

and numerical errors. In comparison, the experimental results are also subject to some other nonidealities. These include geometric error and position error of the coil. Additionally, the measured magnetic field is an average measurement over the area of the coil, which is not identical to the magnetic field in the centre point of the coil. As the coil area decreases, it gives an accurate point measurement of magnetic field. However, the signal induced in the coil is small, leading to the degradation in the quality of data. Therefore, the coil should provide a suitable compromise between accuracy and signal amplitude.

The joint  $L^1$ -TV regularization leads to the improvement in localizing the inhomogeneities for MDEIT. Furthermore, the sharp edges and piecewise constancy of the TV regularization and the sparsity of  $L^1$  penalty may encourage the enhancement in clinical applications. For example, MDEIT may be useful in the detection of cancer which is the localized high impedance tissue. And the sharp impedance contrast between the lung and the surrounding tissues might be better reconstructed by MDEIT. Further simulation studies could be considered and techniques developed to reconstruct images from more complex phantoms. Another application of MDEIT might provide enhancements over current imaging techniques is the dynamic continuous real-time monitoring of the imaging object such as the brain. But MDEIT still struggles to produce images with good resolution that are routine in CT and MRI because of the inherent ill-posedness of MDEIT inverse problem and the measurement system. At the present time, there are two above-mentioned restrictions on the quality of images from the measurements taken on the human subjects. Therefore, the objective of the next phase in the development of MDEIT will be to improve both data collection system and reconstruction methods to enable accurate imaging.

With the present measurement system, we only reconstructed the current density image from the experimental data. Further conductivity image reconstruction of more complex phantoms should be considered. Therefore, the next work is to improve the MDEIT data measurement system, obtaining more accurate magnetic field data.

## ACKNOWLEDGMENT

This work was supported by the Fundamental Research Funds for the Central Universities (No. N141903002), the National Natural Science Foundation of China (No. 61374015, 61202258), the Ph.D. Programs Foundation of Ministry of Education of China (No. 20110042120037).

## REFERENCES

- [1] S. Ahlfors and R. Ilmoniemi, "Magnetic imaging

- of conductivity,” *Proc. 14<sup>th</sup> Ann. Int. Conf. IEEE Eng. Med. Biol. Soc.*, Paris, pp. 1717-1718, 1992.
- [2] J. C. Tozer, R. H. Ireland, D. C. Barber, and A. T. Barker, “Magnetic impedance tomography,” *Ann. N. Y. Acad. Sci.*, vol. 873, pp. 353-359, Apr. 1999.
- [3] R. H. Ireland, J. C. Tozer, A. T. Barker, and D. C. Barber, “Towards magnetic detection electrical impedance tomography: data acquisition and image reconstruction of current density in phantoms and in vivo,” *Physiol. Meas.*, vol. 25, no. 3, pp. 775-796, Jun. 2004.
- [4] R. H. Ireland and D. C. Barber, “Constrained image reconstruction for magnetic detection electrical impedance tomography,” *Int. J. Imag. Syst. Technol.*, vol. 17, no. 6, pp. 379-382, Dec. 2007.
- [5] D. Strong and T. Chan, “Edge-preserving and scale-dependent properties of total variation regularization,” *Inverse Problems*, vol. 19, no. 6, pp. 165-187, 2003.
- [6] L. Hao, G. Li, and L. Xu, “Magnetic detection electrical impedance tomography with total variation regularization,” *Biomed. Mater. Eng.*, vol. 24, no. 6, pp. 2857-2864, 2014.
- [7] D. Donoho, “Compressive sensing,” *IEEE Trans. Inf. Theory*, vol. 52, no. 4, pp. 1289-1306, 2006.
- [8] E. J. Candes and T. Tao, “Near optimal signal recovery from random projections: universal encoding strategies,” *IEEE Trans. Inf. Theory*, vol. 52, no. 12, pp. 5406-5425, 2006.
- [9] G. Oliveri, N. Anselmi, and A. Massa, “Compressive sensing imaging of non-sparse 2d scatterers by a total-variation approach within the born approximation,” *IEEE Transactions on Antennas & Propagation*, vol. 62, no. 10, pp. 5157-5170, 2014.
- [10] D. Joyita, A. Sangtae, L. Changqing, R. C. Simon, and M. L. Richard, “Joint L1 and total variation regularization for fluorescence molecular tomography,” *Physics in Medicine & Biology*, vol. 57, no. 6, pp. 1459-1476, 2012.
- [11] G. Hao and Z. Hongkai, “Multilevel bioluminescence tomography based on radiative transfer equation part 2: total variation and l1 data fidelity,” *Optics Express*, vol. 18, no. 3, pp. 2894-2912, 2010.
- [12] G. Li, L. Hao, R. Chen, and L. Lin, “A new electrode mode for magnetic detection electrical impedance tomography: Computer simulation study,” *IEEE Transactions on Magnetism*, vol. 48, no. 10, pp. 2543-2550, 2010.
- [13] K. D. Andersen, E. Christiansen, A. Conn, and M. L. Overton, “An efficient primal-dual interior-point method for minimizing a sum of Euclidean norms,” *SIAM J. on Scientific Computing*, vol. 22, no. 1, pp. 243-262, 2000.
- [14] A. Borsic, B. M. Graham, A. Alder, and W. R. B. Lionheart, “In vivo impedance imaging with total variation regularization,” *IEEE Transactions on Medical Imaging*, vol. 29, no. 1, pp. 44-54, 2010.
- [15] L. Hao, G. Li, and L. Lin, “Optimization of measurement arrangements for magnetic detection electrical impedance tomography,” *IEEE Transactions on Bio-medical Engineering*, vol. 61, no. 2, pp. 444-452, 2014.